Information Segregating Towards Simultaneous Tracking and Imaging Based on Ghost Imaging

Long-Kun Du,[1,2] Shuai Sun,[1,2,3] Liang Jiang,[1,2] Chen Chang,[1,2] Hui-Zu Lin,[1,2,3] and Wei-Tao Liu[1,2,3,*]

[1] *Institute for Quantum Science and Technology, College of Science, National University of Defense Technology, Changsha 410073, China*

[2] *Interdisciplinary Center of Quantum Information, National University of Defense Technology, Changsha 410073, China*

[3] *Hunan Key Laboratory of Mechanism and technology of Quantum Information, Changsha 410073, China*

(Received 24 August 2022; revised 13 March 2023; accepted 6 April 2023; published 4 May 2023)

Simultaneously tracking and imaging moving objects has been an open problem, due to the requirement on a large amount of information and the low photon flux during the very moment that the object can be taken as stationary. Information of the moving object can be decomposed into motion information of the centroid and image of the object. The amount of motion information can be far less than that for imaging. Therefore, we propose to solve the problem by information segregating. That is, to obtain the motion trajectory and gradually achieve the image during the tracking process. As an example, we unify tracking and imaging within a single system, based on ghost imaging with a four-quadrant detector. The differential signals from the quadrant detector are used for tracking, and the sum signals are for imaging. Experimental results show that our method provides high tracking accuracy and high-quality imaging. For objects of angular velocity up to 165 mrad/s, the tracking accuracy reaches 1/7 of the imaging resolution. Possible influences from different practical factors are also discussed.

DOI: 10.1103/PhysRevApplied.19.054014

I. INTRODUCTION

Observing moving objects within a large field of view is essentially required in a variety of applications, such as autonomous driving [1], traffic monitoring [2], scouting, biomedical imaging [3], and so on. The task can still be tricky with current techniques, since both tracking and imaging are simultaneously required. An immediate action is to obtain a sequence of images, with both trajectory and image of the object achieved [4–7]. However, a large continuous flow of information is required to be handled. For moving objects, high-speed cameras are necessary, which results in excessive hardware requirements and a rather large amount of data in practical applications [8,9]. Another solution is image-free tracking, abandoning the capability of imaging. This can be done by a LiDAR, relying on directional probe beams that can be scanned spatially or angularly [10,11]. Such systems with high spatial accuracy are costly. Meanwhile, the position of the object can also be obtained by spatially encoding the illumination [12–14], with a requirement on high refreshing frequency of such illumination patterns. These image-free methods are limited in applications due to the lack of images.

From the view of information acquisition, the tasks of tracking and imaging can be quite distinct and can be done in parallel. Tracking is continuously acquiring motion of the object's centroid, while imaging obtains its spatial structure. Compared to acquiring a sequence of images, the amount of information required for tracking is relatively tiny [15]. With the centroid of the object being tracked, keeping it within the illumination field by beam steering, the image of the object turns out to be static, which no longer requires a large flow of information. That is, if segregated into a flow of changing positions and a static image, the amount of required information can be greatly reduced.

For this goal, a system with the capability to track and image in parallel, with a detector of few pixels, is required. Ghost imaging (GI) provides a way that can obtain an image with only a single-pixel detector. With GI, the image is reconstructed from second-order correlation between a number of illumination patterns and detection results with a non-spatial-resolving detector, which collects the corresponding echoes [16–21]. Based on its features of high sensitivity [22], strong robustness [23], lensless imaging, GI promises a broad perspective in different applications [24–27], which has also been extended from optics to terahertz wave [28–31], X-ray [32–34], and even material waves [35,36]. Towards moving objects, it was proposed

*wtliu@nudt.edu.cn

to obtain the trajectory by cross-correlation between blurring images from a few hundred samplings. Then both trajectory and image can be gradually obtained, assuming a temporary static object during each momentary sampling process [7,37]. Further, velocity measurement was also demonstrated under the illumination of the translational patterns, thus tracking and imaging can be simultaneously achieved [38], assuming a uniform motion with each momentary sampling procedure. For moving objects of higher speed and diverse motion, such assumptions are expected to be released.

In view of the above analysis, we demonstrate an information segregating method to achieve simultaneous tracking and imaging of a moving object, using a unified system, based on GI with quadrant detection and beam steering. From each echo, displacement of the object can be measured, according to which the illumination beam is steered. Therefore, the object is almost kept relatively static to the imaging system. The images can be obtained from correlation between the illumination patterns and the echoes. Thanks to the small amount of required data, the feedback frequency and tracking accuracy can be rather high. With the angular velocity up to 165 mrad/s, the tracking accuracy can reach 1/7 of the spatial resolution of GI. The field of view is not limited by the immediate illumination area, as a result of beam steering. Besides, no prior information or assumption about the motion is required anymore.

II. METHOD

Generally speaking, the greater the amount of information acquired, the greater the consumption of resources and energy. Nyquist-Shannon's theorem establishes a sufficient condition for sampling rate that permits a discrete sequence of samples to capture a continuous signal of finite bandwidth. For a two-dimensional image with size of L_x, L_y and spatial bandwidths of B_x, B_y in x, y direction, the required information capacity is defined as the spatial bandwidth product (SBP)

$$B_S = 2L_xB_x \times 2L_yB_y, \tag{1}$$

where $B_S = B_{\mathrm{Sx}}B_{\mathrm{Sy}}$ [39]. Under noise, it should be rewritten as [40]

$$C_0 = B_S\log((s+\mu)/\mu) = B_S\log(1+s/\mu), \tag{2}$$

with s being the average power of signal, μ being the power of additive noise. For a signal of duration T and bandwidth B_t, the minimal number of required sampling points is defined as time bandwidth product, $B_T = 2TB_t$. Then, the total information capacity required is [41]

$$C_1 = B_S \times B_T\log(1+s/\mu). \tag{3}$$

In many cases, the object's shape changes slowly or even does not change. The information of the moving object can be decomposed into the spatial image and the movement of the centroid. For the spatial image, the information capacity can be expressed as C_0. For motion, the field of view is much larger than the object, and without prior information, it can be considered that the object can appear anywhere with equal probability. Then, the information of one centroid position can be expressed as $\log(2L_xB_x \times 2L_yB_y) = \log(B_S)$. The information of the centroid changing with time is $B_T\log(B_S)$. Since the motion information and the image information of the object are independent to each other, if obtained segregatedly, the required information capacity will be

$$C_2 = B_S\log(1+s/\mu) + B_T\log(B_S). \tag{4}$$

For fast moving objects, the B_T is large, so $C_2 \ll C_1$, and the resources required can be greatly reduced.

Four-quadrant detectors are often used in tracking scenes, such as laser guidance [42], spot positioning [43], sun tracking [44], and laser diameter measurement [45] etc. However, no image can be obtained. Towards our goal, we build a modified GI system, unifying the capability of tracking and imaging within a simple system. The main idea is shown in Fig. 1(a). For illumination, a sequence of pulses with random spatial patterns are headed onto the object plane by a beam-steering module. For the corresponding echoes, a four-quadrant detector is employed, serving for bucket detection, as well as for determining the displacement of object. As any two-dimensional motion can be decomposed into two degrees of freedom, the differential values of the four-quadrant detector can be sufficient for retrieving displacement and moving direction of the object. The illumination beam is steered to maintain the object located at the center of the illumination area. In parallel, the sum value of all the quadrants reflects the intensity of echo, which offers bucket detection for image reconstruction.

A. Tracking with four-quadrant detection under random illumination patterns

The tracking system is shown in the right part of Fig. 1(a). A four-quadrant detector is placed on the image plane of the objects, as shown in Fig. 1(b). Movement of the object will cause spatial shift of the echo, resulting in nonzero differences between the quadrants. Accordingly, steer the illumination beam to draw the differential signal towards zero, centroid of the object can be kept close to origin of the detector. Suppose the centroid of the object departs from the origin by Δx and Δy, as shown in

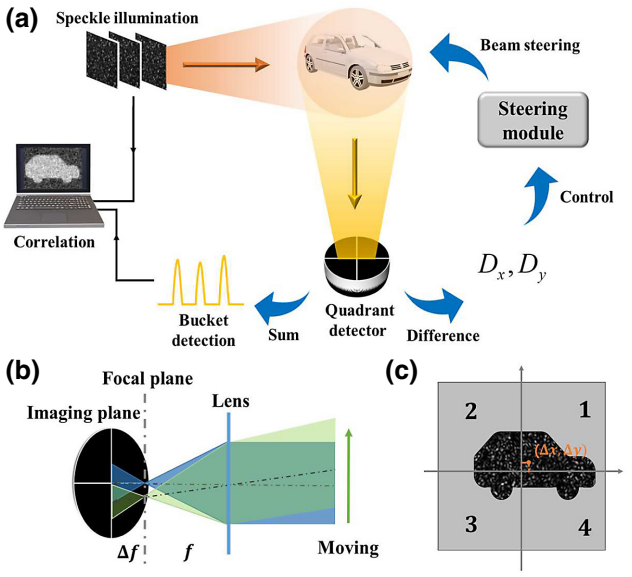

FIG. 1. Main idea of information segregating. The object is illuminated by speckle patterns and imaged on the surface of a quadrant detector, the results of which are separately used for tracking and imaging.

Fig. 1(c). The normalized differential signal corresponding to x direction can be written as

$$D_x = \frac{(s_1+\mu_1)+(s_4+\mu_4)-(s_2+\mu_2)-(s_3+\mu_3)}{\langle s_s+\mu_s\rangle}, \\ = \frac{s_1+s_4-s_2-s_3}{\langle s_s+\mu_s\rangle}+\frac{\mu_1+\mu_4-\mu_2-\mu_3}{\langle s_s+\mu_s\rangle}. \quad (5)$$

Here s_i and $\mu_i (i=1,2,3,4)$ denote the signal and noise in the ith quadrant, respectively. And $s_s=\sum s_i$, $\mu_s=\sum \mu_i$. $\langle\cdot\rangle$ denotes ensemble averaging. Similarly, D_y represents the normalized differential signal in y direction. With no loss of generality, only one dimension is analyzed.

Take the area of lighted spot on the four-quadrant detector as S, and the length falling on the centerline of the detector as l. With a small displacement, $\Delta x \ll l$, we can obtain the expectation of D_x as $\langle D_x\rangle = [(S/2+\Delta x l)-(S/2-\Delta x l)]/S = 2\Delta x l/S$. So within a certain interval,

$$\Delta x = \frac{S\langle D_x\rangle}{2l} \propto \langle D_x\rangle . \quad (6)$$

Since the differential signal is proportional to Δx, it can be used for tracking. Keeping $\langle D_x\rangle$ equal to zero all the time, the centroid of moving object will be kept at the origin of the four-quadrant detector.

In our method, the differential signal is not only determined by movement of the object, but also the fluctuation of random illumination. Considering the fluctuations caused by speckle illumination and detection noise, the variance of D_x is (see Sec. 1 in the Appendix for details)

$$\Delta^2 D_x = \frac{\sum_{i=1}^{n}\bar{I}_i^{\,2}+4\sigma^2}{\langle s_s+\mu_s\rangle^2}, \quad (7)$$

where $\bar{I}_i$ is the echo intensity of the ith speckle on the object and σ^2 is the variance of detection noise from each quadrant. Disregarding detection noise, the error caused by speckle fluctuations can be controlled within average size of one speckle in a single detection (refer to Sec. 1 in the Appendix for details). n is the number of speckles within the area of the object, which can be roughly estimated via the echo signals (see Sec. 4 within the Appendix for details).

To keep the object properly tracked, the differential signals in the x and y directions are fed into the control program to control the steering module. The accuracy of tracking is mainly affected by two factors. One is the intensity fluctuations of illumination patterns and noise. The other is the displacement within the duration that the object is not illuminated, namely the sampling interval.

Suppose the repetition frequency of illumination pulses is f_c, which can also be the tracking frequency, and the bandwidth of detector is high enough for such pulses. For an object moving at a speed of v, with the sampling interval of $1/f_c$, the displacement is v/f_c. The change of $\langle D_x\rangle$ is

$$\delta\langle D_x\rangle = \frac{2v\sqrt{n\bar{I}}}{f_c\langle s_s\rangle} = \frac{2v}{\sqrt{n}df_c}, \quad (8)$$

where d is the average size of the speckles. The higher the tracking frequency f_c, the higher the tracking accuracy. The error in tracking $\delta\Delta x$ is comprised of the detection error and the sampling interval error, as

$$\delta\Delta x \propto \sqrt{\frac{\sum_{i=1}^{n}\bar{I}_i^{\,2}+4\sigma^2}{\langle s_s+\mu_s\rangle^2}+\frac{4v^2}{nd^2{f_c}^2}}. \quad (9)$$

The first item in Eq. (9) means the error of detection. The noise can be described by a Gaussian distribution with zero mean, so $\langle\mu_s\rangle = 0$. Here we define the detection signal-to-noise ratio (DSNR) as $\mathrm{DSNR} = \langle s_s\rangle / \sqrt{\sum_{i=1}^{n}\bar{I}_i^{\,2}+4\sigma^2}$. The second term in Eq. (9) reflects the influence of the motion speed v and the required tracking frequency f_c. If the tracking accuracy is expected to be δ_0, i.e., $\delta\Delta x \le \delta_0$, f_c is required to satisfy

$$f_c \ge k\frac{2v}{\sqrt{nd^2[{\delta_0}^2-(\sum_{i=1}^{n}\bar{I}_i^{\,2}+4\sigma^2)/\langle s_s\rangle^2]}}, \quad (10)$$

where k is a scale factor, which is determined by the geometric configuration and the photoelectric response of the

system. So the faster the object moves, the higher the tracking frequency is required to maintain the same tracking accuracy. Thanks to the small amount of data for quadrant detection, the tracking frequency can be rather high.

B. Imaging with quadrant detection

For imaging, as shown on the left part of Fig. 1(a), the sum of four quadrants is used as the bucket detection I_b. The image can be obtained through the correlation between I_b and the illumination patterns $I_r(\vec{x})$ as [46]

$$G(\vec{x}) = \langle \Delta I_r(\vec{x}) \Delta I_b \rangle , \tag{11}$$

where $\Delta I_r(\vec{x}) = I_r(\vec{x}) - \langle I_r(\vec{x}) \rangle$, $\Delta I_b = I_b - \langle I_b \rangle$. In order to keep the imaging results free from motion blurring, the displacement of the object is expected no exceeding the spatial resolution within the imaging duration [47]. With the tracking method discussed above, it can be obtained that the tracking error caused by speckle fluctuations can be controlled within size of one speckle, even using one single detection for tracking (see Sec. 1 within the Appendix). In ghost imaging, the spatial resolution equals the average size of speckles. Therefore, under four-quadrant tracking, the image can be reconstructed with no motion blur. To measure the quality of the image, contrast-to-noise ratio (CNR) is usually calculated as [48]

$$C_{\mathrm{nr}} = \frac{\langle G(\vec{x}_{\mathrm{in}}) \rangle - \langle G(\vec{x}_{\mathrm{out}}) \rangle}{\sqrt{\Delta^2 G(\vec{x}_{\mathrm{in}}) + \Delta^2 G(\vec{x}_{\mathrm{out}})}}, \tag{12}$$

where $\vec{x}_{\mathrm{in}}$ represents the area occupied by the object within the illumination area, called object region, and $\vec{x}_{\mathrm{out}}$ represents the rest of the area, called background region, with $\Delta^2 G$ being the corresponding variance. A larger CNR implies a higher quality of imaging results.

III. EXPERIMENTS AND RESULTS

To test the performance of this method, we demonstrate an experimental setup as shown in Fig. 2. The system is shown within the blue dotted line, with a high reflection mirror (HRM) serving as transmitter and receiver. The distance between the object and the system is 65 cm. Random speckle patterns, generated by lighting a pulsed laser (DHNL 1064-50-P-N-M-FA) on a rotating ground glass, are illuminated onto the object's surface. A four-quadrant detector is placed on the image surface to collect the echo signals. To enable the system for tracking, the HRM is jointly driven by two turntables: a vertical motorized swing stage (Zolix: PSAG 15-195) and a horizontal motorized rotary stage (Zolix: TBRK 100). The displacement of the object can be taken as proportional to the rotation angle of the turntable (see Sec. 2 within the Appendix). According to Sec. II A, movement of the object will bring changes in

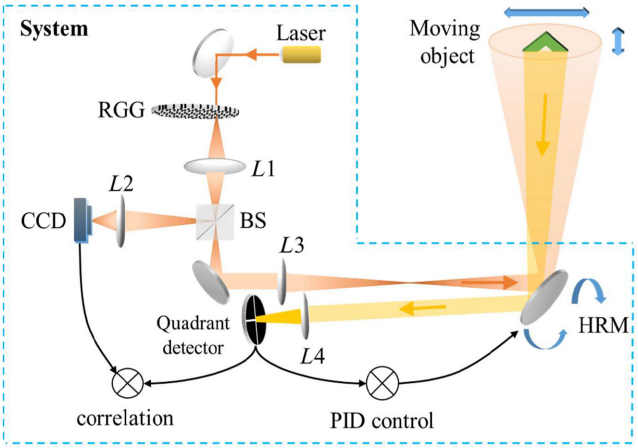

FIG. 2. Experimental setup. A pulsed laser beam (1064 nm) passes through a rotating ground glass (RGG) to form a rapidly changing speckle field, which is then split into two beams by a beam splitter (BS). One beam is recorded by a CCD, and the other beam is headed onto the object via an imaging lens $L3$ and a HRM. Light reflected by the object returns through the same path and is collected by the lens $L4$. The four-quadrant detector (First Sensor:QA4000-10) is placed on the image plane of the lens $L4$ to determine the spatial centroid of the echoes. The differential signal is sent to a steering module to track the object, and the sum of four quadrant is used as bucket detection to obtain a ghost image of the object.

D_x and D_y of the four-quadrant detection. Then the differential signals are sent to a proportion-integral-differential (PID) program. Speed and acceleration of the movement can be estimated via PID, with the output converted into driving pulses by a direct digital synthesis (DDS) towards the stepper motors. By carefully setting the parameters, the beam can be steered properly to keep the object in the center of the illuminated area. From the actions of the motors, the trajectory of the object can be obtained. At the same time, the illumination patterns are recorded by a CCD, as shown in Fig. 2, on the reference arm. The image of the object can be acquired through correlation between the sum of four-quadrant detection and the corresponding recorded patterns.

The tracking and imaging results are shown in Fig. 3. Figures 3(a) and 3(b) show the measured trajectories and real trajectories of a "bird" (cut out of a plain piece of white paper), and a *c*-type metal bracket (one piece of ESK16 by Thorlabs), denoted as "bird" and "*C*," respectively, both of which have rough surfaces. The red curve shows the actual trajectory of the object captured by another monitoring camera (not shown in Fig. 2), and the blue curve is the measured trajectory obtained by our method. The object is driven by a two-dimensional motion system consisting of horizontal (Zolix: PSA 100-11-X) and vertical (Zolix: PSA 100-11-Z) translation stages. The velocity on both the

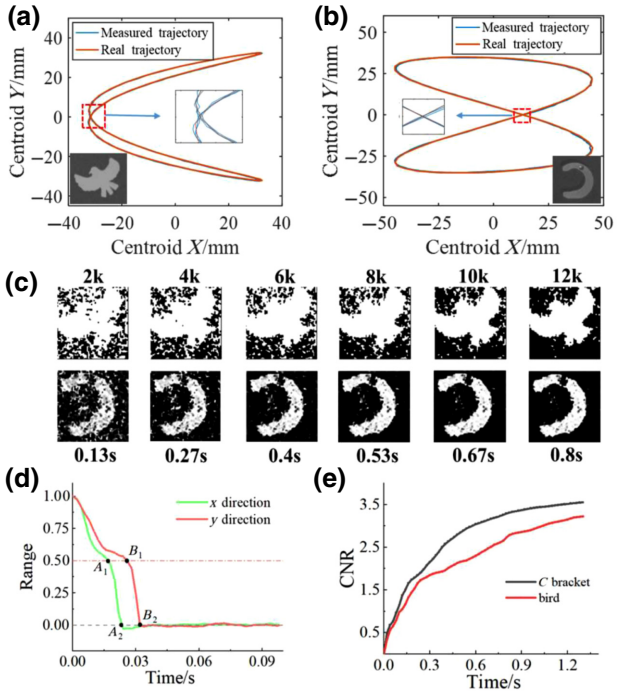

FIG. 3. Results of tracking and imaging. (a) Trajectory of the white paper "bird." The maximum movement speed of the object in the horizontal and vertical direction are 7.15 cm/s and 3.58 cm/s. (b) Trajectory of the metal bracket "*C*." The maximum movement speed of the object in the horizontal and vertical directions are 10.7 cm/s and 4.2 cm/s. (c) Evolution of imaging results during tracking. (d) Temporal response of tracking in x and y direction. To test this, the object is first set at the edge of the illuminated area (1.0 on the vertical axis). Then the beam is steered such that the object is kept at the center (0 on the vertical axis). (e) Image quality varies with time.

horizontal and vertical axes varies sinusoidally with time:

$$V_x = a\sin(\omega_1 t + \phi_1),$$
$$V_y = b\sin(\omega_2 t + \phi_2). \tag{13}$$

To compare the measured trajectory and the real one, we calculate the root-mean-square error (RMSE) between them, where RMSE is used to measure the tracking accuracy. The smaller the RMSE, the higher the tracking accuracy. Trajectory of bird is shown in Fig. 3(a). The size of the bird is 2.8 cm × 1.9 cm, and the range of horizontal and vertical movement are $L_x = L_y = 6.5$ cm. The maximum speed of the object in the horizontal and vertical directions are $a = 7.15$ cm/s and $b = 3.58$ cm/s, respectively. RMSEs of tracking on the horizontal and vertical directions are 0.027 cm and 0.016 cm, respectively. The trajectory of *C* is shown in Fig. 3(b). The object is 2.0 cm × 2.4 cm in size and moving within an area of $L_x = 9.0$ cm, $L_y = 7.0$ cm, with the maximum speed being $a = 10.7$ cm/s and $b = 4.2$ cm/s. At this time, the composite motion speed of the object is close to $\sqrt{a^2 + b^2} = 11.5$ cm/s. The maximum angular velocity in the x direction is approximately 165 mrad/s. RMSEs of the *C* are 0.024 cm and 0.017 cm in horizontal and vertical, respectively. The average diameter of speckles on the object plane is 0.20 cm, which is also the imaging resolution. From the experiments, the average tracking error is smaller than 1/7 of that.

In Fig. 3, the refresh rate of illuminated speckle patterns is 15 kHz, and the tracking frequency is set as 2 kHz, data for which is picked at equal intervals from the echo signals. The illumination area is a circle with a diameter of 5.0 cm, and the range of motion has dramatically exceeded that size. Evolution of the imaging results within 0.8 s is shown in Fig. 3(c). The first row is the imaging results of the bird, and the second row is that of the *C*. Since the tracking accuracy is higher than the spatial resolution, there is almost no motion blur.

Figure 3(d) shows the process from the entry of an object to being stably tracked, with the moving range normalized by the size of illumination area. Namely, 1.0 means the object is on the edge of the illumination area, while 0 refers to the object located at the center of the area. The green and red lines represent the tracking process in x and y directions. We define the time it takes from 1.0 to 0 as the "tracking response time." It is 0.023 and 0.032 s, from the start to A_2 and B_2, in x and y directions. The difference in tracking response time is caused by the difference in sensitivity of the stepper motors. The tracking response time is so short that the motion of the object during such time is even negligible. So the tracking system can lock on the object immediately by beam steering. From Fig. 3(d), the tracking process is slower at first and then faster, with a knee point at $A_1(B_1)$. The reason lies in the response of PID. When the object is moving from the edge to the middle of the illumination area, the absolute value of the differential signal increases first until the whole object is imaged onto the detector, and then decreases. Figure 3(e) shows the image quality measured by CNR during the tracking process. The red and black lines represents CNR of bird and *C*, respectively. It increases with imaging time or the number of samplings, while the increase gets slower. This is consistent with the characteristics of ghost imaging.

We also experimentally verify the effect of various factors on the tracking accuracy in Eq. (9). To make action of beam steering smoother, without adding the requirement on data storage, exponential moving average is employed in the experiment. A weighting coefficient α is used, which actually determines the number N of effectively averaged samplings and can be approximated as $\alpha \approx 1/N$ (see Sec. 3 within the Appendix for details). Since the two dimensions are essentially equivalent, experiments are only done in x direction, and the results are shown in Fig. 4. We estimate the influence of tracking frequency, speed of the object, DSNR, and the weighting coefficient α, with RMSE as a measure. For each data point, the mean value

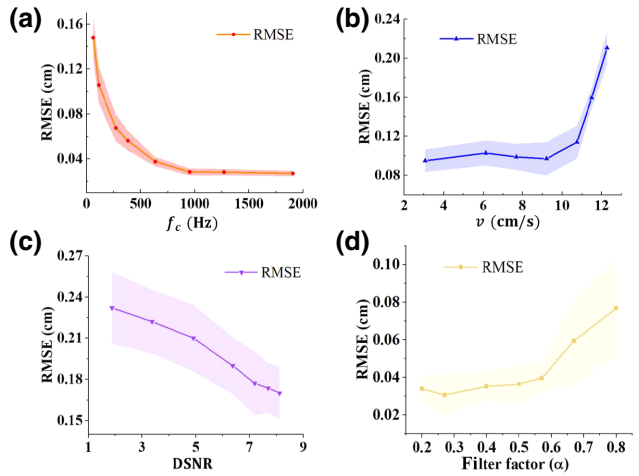

FIG. 4. Variation of tracking accuracy in the experiments. The RMSE between measured trajectory and the real one is taken to measure tracking accuracy. The factors including the tracking frequency f_c, speed of the object v, the DSNR, and the weighting coefficient α, are considered. Data for each point is obtained from statistics over 10 times of experiments. The object moves sinusoidally with a maximum velocity of 10.7 cm/s for (a),(c),(d). The tracking frequency is 100 Hz for (b),(c), and 1000 Hz for (d).

and error bar are achieved from statistics over 10 times of experiments, and the object moves sinusoidally for these tests.

The effect of tracking frequency f_c is shown in Fig. 4(a). When f_c is small, improvement in tracking frequency provides significant enhancement in accuracy. While, such a trend slows down with higher tracking frequency. When f_c reaches 1000 Hz, the tracking accuracy almost approaches the limit of our system, with RMSE remaining basically the same. For $f_c = 1907$ Hz, RMSE drops to 0.027 cm. Figure 4(b) shows RMSE for different velocities, with $f_c = 100$ Hz. The maximum speed changes from 3 to 11.5 cm/s. With a given tracking frequency, the current system can work for a range of motion speeds. As a result, RMSE increases slowly then rises rapidly when the speed exceeds 10 cm/s. That means in our setup, 10 cm/s is the upper limit under this particular tracking frequency. In addition, signal-to-noise of detection also affects the performance of tracking. Experimental results under different DSNRs are shown in Fig. 4(c). Under certain detection noise, DSNR is changed by adjusting the intensity of illumination light. With the improvement of DSNR, RMSE decreases steadily, indicating that higher DSNR offers higher tracking accuracy. The influence of α on tracking accuracy is shown in Fig. 4(d). The smaller the coefficient α, the more useful raw data is weighted within a fixed time, so the tracking is more accurate (see Sec. 3 within the Appendix for details).

From the above results, we verify our approach of information segregating by demonstrating tracking and imaging of moving object, with the influence of each factor being consistent with the theoretical analysis. Limited by currently used hardware, the speed of the tracked object is not very high. For no-live load, the maximum angular velocity is 8°/s for the vertical stage and 20°/s for the horizontal one. Considering the load and acceleration in motion, we almost reach the speed limit of our experimental system. The bandwidth of the four-quadrant detector used here can be very high (up to dozens of MHz), allowing for efficient data processing. Using devices of higher rotation speed and response bandwidth, such as galvanometer mirrors, will offer substantial enhancement in tracking capability. Therefore, making our method promising for fast-moving objects.

In practice, our method can be applied to track and image objects, such as aircraft, ships, etc. Utilizing Radar or other methods to achieve the discovery of the object, our method can provide more precise tracking and clear imaging upon scanning within a small range. In our experiments, although the absolute speed realized is not very fast, the current angular tracking velocity can be useful. The maximum angular velocity is 165 mrad/s, which is higher than most reported results using ghost imaging. It means that the speed of object can be as high as 16.5 m/s, if the object is at a distance of 100 m, and 165 m/s for a distance of 1 km. That is, the current level we achieve can be of practical significance.

For the signals used for tracking, we use exponential average filtering. With optimized data-filtering method or tracking strategy, performance of tracking might also be further improved. Besides, the effect caused by illumination fluctuations is as small as the size of one speckle owing to the fact that the statistics of random speckle patterns are translation invariant in space. Other illumination patterns may also be useful, with further study. Since the experiments are demonstrated with a typical GI system, those existing methods developed for enhancing GI can also be introduced for further improvement. First, the time-correlation method is used to improve the signal-to-noise ratio in this work, which improves the quality of reconstructed images [49]. Based on that, the longitudinal motion can be measured, so the tracking of three-dimensional movement could be realized. Second, the sum signal of the four-quadrant detector is used as the bucket detection. If the signal of every single quadrant is correlated with the reference arm, a quarter of the image can be obtained, then the overall image can be obtained by combining the four quarters [50]. This might help to improve the imaging quality of GI. Also, using developed algorithms, such as compressed sensing and machine learning [51,52], the quality of images might be improved, even with fewer samplings. Here we perform an example of information segregating. For information acquisition, better designed segregating methods will lead to better performance and broader applications.

IV. CONCLUSION

Towards information acquisition of moving objects, we propose information segregating in this paper. The total information of a large amount is uncoupled into a much smaller flow (motion of centroid) and a static structure (image of the object), and treated separately. By detecting the displacement of the centroid, the motion information is fed back to a beam-steering module for tracking. Thus, the object is kept static with respect to the imaging system. As an example, we verify our method with a ghost-imaging system based on four-quadrant detection. Simultaneous tracking and imaging of moving objects are achieved. By beam steering, the tracked motion range can be far beyond the immediate illumination area. And the tracking accuracy in our experiments is below 1/7 of the imaging resolution, even with the angular speed up to 165 rmad/s.

Photoelectric detectors featuring large-scale pixels usually have a limited frame rate and sensitivity, making the performance of the image-based tracking method still quite modest. While, ghost imaging allows for extracting information from even a small number of photons. Combining our approach of information segregation, it becomes possible to achieve tracking and imaging for moving objects, even under weak signals. By hierarchically organizing and utilizing information of different categories, information acquisition, and processing become much more efficient. As a result, this approach is promising for fast-moving objects. Furthermore, the idea of information segregating can be spread to multiple practical applications.

ACKNOWLEDGMENTS

This work is supported by the National Natural Science Foundation of China under Grants No. 62105365, No. 62001484, and No. 62275270.

APPENDIX

1. Measurement errors due to speckle fluctuations and noise

In Sec. II, we get D_x expressed as Eq. (5). D_x can be divided into the the signal part D_{x1} and the noise part D_{x2}, with $D_{x1} = (s_1 + s_3 - s_2 - s_4)/\langle s_s + \mu_s \rangle$ and $D_{x2} = (\mu_1 + \mu_3 - \mu_2 - \mu_4)/\langle s_s + \mu_s \rangle$. The noise can be regarded as obeying the Gaussian distribution with variance σ^2, and the noise level in the four quadrants is the same. Then $\langle D_{x2} \rangle = 0$ and $\Delta^2 D_{x2} = (\sigma_1^2 + \sigma_2^2 + \sigma_3^2 + \sigma_4^2)/\langle s_s + \mu_s \rangle = 4\sigma^2/\langle s_s + \mu_s \rangle^2$. For D_{x1}, the intensity obeys the negative exponential distribution in both time and space domain for random speckle illumination. For a point on the object, the echo intensity also obeys the negative exponential distribution $f(I) = e^{-I/\bar{I}}/\bar{I}$, where $\bar{I}$ is the average value of the echo intensity. Therefore, the variance of echo intensity is $\Delta^2 I = \bar{I}^2$. For the number of speckles n occupied by the object, the variance of the signal is $\Delta^2 D_{x1} = \sum_{i=1}^{n} \bar{I}_i^2 / \langle s_s + \mu_s \rangle^2$. $\Delta^2 D_x = \Delta^2 D_{x1} + \Delta^2 D_{x2}$, then $\Delta^2 D_x$ is obtained as Eq. (7).

Furthermore, for ghost-imaging results to be smear-free, the displacement of the object is expected to not exceed the size of speckles [47]. As Fig. 1(c) shows, the number of speckles on the centerline of a four-quadrant detector is approximately $\sqrt{n}$. When displacement of the object equals the average size of one speckle, disregarding noise, the differential signal is $2\sqrt{n}\bar{I}/\langle s_s \rangle$. So if $2\sqrt{\Delta^2 D_x'} \leq 2\sqrt{n}\bar{I}/\langle s_s \rangle$, error of Δx has a probability of 95 % to appear within one speckle. For $2\sqrt{n\bar{I}^2/(N\langle s_s \rangle^2)} \leq 2\sqrt{n}\bar{I}/\langle s_s \rangle$, it requires $N \geq 1$, where N is the number of samples. That is, in the case of single detection, the tracking error caused by speckle fluctuations is limited within one speckle.

2. Measurement of displacement

In Fig. 2, the high-reflection mirror (HRM) is driven by turntables to track the object. It has two rotational degrees of freedom, horizontal and vertical, as shown in Fig. 5. Suppose position of HRM is in the middle of a sphere, and the motion plane of the object is represented with the green plate. The red arrow represents the direction of the light field projection. By rotating HRM, the projected light field moves along with the object so that the object is always kept in the middle of the light field. The rotation angles in the horizontal and vertical directions are θ and ϕ, respectively. Then the motion trajectory on the object plane is $x = L\tan\phi/\cos\theta$ and $y = L\tan\theta$, where L is the distance between the center of HRM and the object plane. When $\theta, \phi \ll 1$, the above formula can be expressed as $x = L\phi$, $y = L\theta$, so the displacement of an object can be considered to be proportional to the rotation angle of the turntable.

3. The effect of weighting coefficient α

We use the exponential moving average method in the experiments. For the ith collected raw data D_i, the value after exponential moving average is $d_i = \alpha D_i + (1-\alpha)d_{i-1}$, with $d_1 = \alpha D_1$. The relationship between the

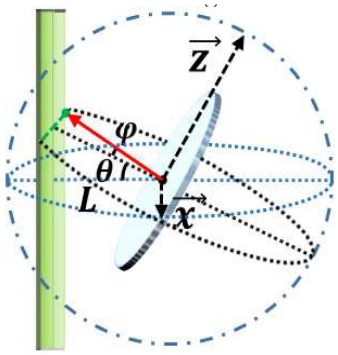

FIG. 5. Schematic diagram of tracking using a rotating HRM.

averaged data and the raw data is

$$d_i = \alpha D_i + \alpha(1-\alpha)D_{i-1} + \alpha(1-\alpha)^2 D_{i-2} + \cdots, \tag{A1}$$

which is the weighted sum of the raw data, and this weight is related to the value of α. When the coefficient of the term is smaller than $1/e$ of the first term $\alpha(1-\alpha)^j < \alpha/e$, the effect of the term on the final result is negligible. At this point, the effective number of terms $N \approx 1/\alpha$. The smaller α, the more useful raw data is weighted. We can simply describe this result by averaging. If the differential signal $D_x{}'$ is achieved after averaging over N raw samples, $\left\langle D_x{}' \right\rangle = \langle D_x \rangle$ and $\Delta^2 D_x{}' = \Delta^2 D_x/N$. It means that the displacement value after exponential moving average can be more accurate.

4. Estimate *n* from the signal

Based on the bucket signals, we can roughly estimate the number of speckles n occupied by the object, which also corresponds to the object's size. Without the object, the mean and variance of the signal are $\langle I_b \rangle = \langle \mu_s \rangle$ and $\Delta^2 I_b = 4\sigma^2$. With object, the mean and variance of the signal becomes $\left\langle I_b' \right\rangle = \langle \mu_s \rangle + n\bar{I}$, $\Delta^2 I_b' = 4\sigma^2 + n\bar{I}^2$. So we can get the number of speckles occupied by the object as $n = (\left\langle I_b' \right\rangle - \langle I_b \rangle)^2/(\Delta^2 I_b' - \Delta^2 I_b)$.

[1] J. Levinson, J. Askeland, J. Becker, J. Dolson, D. Held, S. Kammel, J. Z. Kolter, D. Langer, O. Pink, and V. Pratt, in *2011 IEEE Intelligent Vehicles Symposium (IV)* (Baden-Baden, Germany, 2011), p. 163.

[2] J. Zhou, D. Gao, and D. Zhang, Moving vehicle detection for automatic traffic monitoring, IEEE Trans. Veh. Technol. **56**, 51 (2007).

[3] S. T. Acton and N. Ray, Biomedical image analysis: Tracking, Synthesis Lectures on Image, Video, and Multimedia Processing **2**, 1 (2006).

[4] M.-S. Wei, F. Xing, and Z. You, A real-time detection and positioning method for small and weak targets using a 1D morphology-based approach in 2D images, Light: Sci. Appl. **7**, 18006 (2018).

[5] O. S. Magana-Loaiza, G. A. Howland, M. Malik, J. C. Howell, and R. W. Boyd, Compressive object tracking using entangled photons, Appl. Phys. Lett. **102**, 231104 (2013).

[6] S. Sun, H.-Z. Lin, Y.-K. Xu, J.-H. Gu, and W.-T. Liu, Tracking and imaging of moving objects with temporal intensity difference correlation, Opt. Express **27**, 27851 (2019).

[7] S. Sun, J.-H. Gu, H.-Z. Lin, L. Jiang, and W.-T. Liu, Gradual ghost imaging of moving objects by tracking based on cross correlation, Opt. Lett. **44**, 5594 (2019).

[8] M. El-Desouki, M. Jamal Deen, Q. Fang, L. Liu, F. Tse, and D. Armstrong, CMOS image sensors for high speed applications, Sensors **9**, 430 (2009).

[9] L. Gao, J. Liang, C. Li, and L. V. Wang, Single-shot compressed ultrafast photography at one hundred billion frames per second, Nature **516**, 74 (2014).

[10] U. Wandinger, in *Lidar* (Springer, New York, 2005), p. 1.

[11] F. Daum and R. Fitzgerald, Decoupled Kalman filters for phased array radar tracking, IEEE Trans. Automat. Contr. **28**, 269 (1983).

[12] Z. Zhang, J. Ye, Q. Deng, and J. Zhong, Image-free real-time detection and tracking of fast moving object using a single-pixel detector, Opt. Express **27**, 35394 (2019).

[13] Q. Deng, Z. Zhang, and J. Zhong, Image-free real-time 3-D tracking of a fast-moving object using dual-pixel detection, Opt. Lett. **45**, 4734 (2020).

[14] L. Zha, D. Shi, J. Huang, K. Yuan, W. Meng, W. Yang, R. Jiang, Y. Chen, and Y. Wang, Single-pixel tracking of fast-moving object using geometric moment detection, Opt. Express **29**, 30327 (2021).

[15] G. T. Di Francia, Degrees of freedom of an image, JOSA **59**, 799 (1969).

[16] T. B. Pittman, Y. H. Shih, D. V. Strekalov, and A. V. Sergienko, Optical imaging by means of two-photon quantum entanglement, Phys. Rev. A **52**, R3429 (1995).

[17] R. S. Bennink, S. J. Bentley, and R. W. Boyd, "Two-Photon" Coincidence Imaging with a Classical Source, Phys. Rev. Lett. **89**, 113601 (2002).

[18] J. H. Shapiro, Computational ghost imaging, Phys. Rev. A **78**, 061802 (2008).

[19] F. Ferri, D. Magatti, L. A. Lugiato, and A. Gatti, Differential Ghost Imaging, Phys. Rev. Lett. **104**, 253603 (2010).

[20] J. H. Shapiro and R. W. Boyd, The physics of ghost imaging, Quantum Inf. Process. **11**, 949 (2012).

[21] C. Zhao, W. Gong, M. Chen, E. Li, H. Wang, W. Xu, and S. Han, Ghost imaging LIDAR via sparsity constraints, Appl. Phys. Lett. **101**, 141123 (2012).

[22] P. A. Morris, R. S. Aspden, J. E. Bell, R. W. Boyd, and M. J. Padgett, Imaging with a small number of photons, Nat. Commun. **6**, 1 (2015).

[23] Y.-K. Xu, W.-T. Liu, E.-F. Zhang, Q. Li, H.-Y. Dai, and P.-X. Chen, Is ghost imaging intrinsically more powerful against scattering?, Opt. Express **23**, 32993 (2015).

[24] W. Chen and X. Chen, Object authentication in computational ghost imaging with the realizations less than 5% of Nyquist limit, Opt. Lett. **38**, 546 (2013).

[25] Y. Klein, O. Sefi, H. Schwartz, and S. Shwartz, Chemical element mapping by *x*-ray computational ghost fluorescence, Optica **9**, 63 (2022).

[26] S.-C. Chen, Z. Feng, J. Li, W. Tan, L.-H. Du, J. Cai, Y. Ma, K. He, H. Ding, Z.-H. Zhai, Z.-R. Li, C.-W. Qiu, X.-C. Zhang, and L.-G. Zhu, Ghost spintronic tHz-emitter-array microscope, Light: Sci. Appl. **9**, 1 (2020).

[27] L. Olivieri, J. S. T. Gongora, L. Peters, V. Cecconi, A. Cutrona, J. Tunesi, R. Tucker, A. Pasquazi, and M. Peccianti, Hyperspectral terahertz microscopy via nonlinear ghost imaging, Optica **7**, 186 (2020).

[28] R. I. Stantchev, X. Yu, T. Blu, and E. Pickwell-MacPherson, Real-time terahertz imaging with a single-pixel detector, Nat. Commun. **11**, 1 (2020).

[29] J. S. Totero Gongora, L. Olivieri, L. Peters, J. Tunesi, V. Cecconi, A. Cutrona, R. Tucker, V. Kumar, A. Pasquazi,

and M. Peccianti, Route to intelligent imaging reconstruction via terahertz nonlinear ghost imaging, Micromachines **11**, 521 (2020).

[30] V. Cecconi, V. Kumar, A. Pasquazi, J. S. T. Gongora, and M. Peccianti, Nonlinear field-control of terahertz waves in random media for spatiotemporal focusing, Open Res. Europe **2**, 32 (2022).

[31] R. I. Stantchev, D. B. Phillips, P. Hobson, S. M. Hornett, M. J. Padgett, and E. Hendry, Compressed sensing with near-field tHz radiation, Optica **4**, 989 (2017).

[32] J. Cheng and S. Han, Incoherent Coincidence Imaging and its Applicability in *x*-Ray Diffraction, Phys. Rev. Lett. **92**, 093903 (2004).

[33] N. Radwell, K. J. Mitchell, G. M. Gibson, M. P. Edgar, R. Bowman, and M. J. Padgett, Single-pixel infrared and visible microscope, Optica **1**, 285 (2014).

[34] A. Schori and S. Shwartz, *X*-ray ghost imaging with a laboratory source, Opt. Express **25**, 14822 (2017).

[35] S. Li, F. Cropp, K. Kabra, T. J. Lane, G. Wetzstein, P. Musumeci, and D. Ratner, Electron Ghost Imaging, Phys. Rev. Lett. **121**, 114801 (2018).

[36] R. I. Khakimov, B. M. Henson, D. K. Shin, S. S. Hodgman, R. G. Dall, K. G. H. Baldwin, and A. G. Truscott, Ghost imaging with atoms, Nature **540**, 100 (2016).

[37] W.-T. Liu, S. Sun, H.-K. Hu, and H.-Z. Lin, Progress and prospect for ghost imaging of moving objects, Laser Optoelectron. Prog. **58**, 1011001 (2021).

[38] S. Sun, H.-K. Hu, Y.-K. Xu, Y.-G. Li, H.-Z. Lin, and W.-T. Liu, Simultaneously Tracking and Imaging a Moving Object Under Photon Crisis, Phys. Rev. Appl. **17**, 024050 (2022).

[39] J. W. Goodman, *Introduction to Fourier Optics* (Roberts and Company Publishers, Greenwood Village, 2005).

[40] C. E. Shannon, A mathematical theory of communication, The Bell System Technical Journal **27**, 379 (1948).

[41] I. J. Cox and C. J. R. Sheppard, Information capacity and resolution in an optical system, JOSA A **3**, 1152 (1986).

[42] J. Q. Zhang, F. Xie, Q. S. Xue, and J. X. Xin, Laser guided lens based on four-quadrant detector, Chin. Opt. **8**, 471 (2015).

[43] W. Zhang, W. Guo, C. Zhang, and S. Zhao, An improved method for spot position detection of a laser tracking and positioning system based on a four-quadrant detector, Sensors **19**, 4722 (2019).

[44] P. Roth, A. Georgiev, and H. Boudinov, Design and construction of a system for sun-tracking, Renewable Energy **29**, 393 (2004).

[45] T. W. Ng, H. Y. Tan, and S. L. Foo, Small Gaussian laser beam diameter measurement using a quadrant photodiode, Opt. Laser Technol. **39**, 1098 (2007).

[46] A. Gatti, E. Brambilla, M. Bache, and L. A. Lugiato, Ghost Imaging with Thermal Light: Comparing Entanglement and Classical Correlation, Phys. Rev. Lett. **93**, 093602 (2004).

[47] H. Li, J. Xiong, and G. Zeng, Lensless ghost imaging for moving objects, Opt. Eng. **50**, 127005 (2011).

[48] K. W. C. Chan, M. N. O'Sullivan, and R. W. Boyd, High-order thermal ghost imaging, Opt. Lett. **34**, 3343 (2009).

[49] D. Li, D. Yang, S. Sun, Y.-G. Li, L. Jiang, H.-Z. Lin, and W.-T. Liu, Enhancing robustness of ghost imaging against environment noise via cross-correlation in time domain, Opt. Express **29**, 31068 (2021).

[50] M.-J. Sun, H.-Y. Wang, and J.-Y. Huang, Improving the performance of computational ghost imaging by using a quadrant detector and digital micro-scanning, Sci. Rep. **9**, 4105 (2019).

[51] O. Katz, Y. Bromberg, and Y. Silberberg, Compressive ghost imaging, Appl. Phys. Lett. **95**, 131110 (2009).

[52] F. Wang, C. Wang, C. Deng, S. Han, and G. Situ, Single-pixel imaging using physics enhanced deep learning, Photonics Res. **10**, 104 (2022).